

Electronic Supplementary Material (ESI) for Energy & Environmental Science.
This journal is © The Royal Society of Chemistry 2024

Supporting Information

Self-healing Ion-conducting Elastomer towards Record Efficient Flexible Perovskite Solar Cells with Excellent Recoverable Mechanical Stability

Tangyue Xue,^{‡a,b} Baojin Fan,^{‡c} Ke-Jian Jiang,^b Qiang Guo,^a Xiaotian Hu,^{*c} Meng Su,^b Erjun Zhou^{*a,d} and Yanlin Song^{*b}

^a Henan Institute of Advanced Technology, Zhengzhou University, Zhengzhou 450001, P. R. China. E-mail: zhovej@nanoctr.cn

^b Key Laboratory of Green Printing, Institute of Chemistry Chinese Academy of Sciences (ICCAS), Beijing 100190, P. R. China. E-mail: ylsong@iccas.ac.cn

^c Institute of Polymers and Energy Chemistry, Nanchang University, Nanchang 330031, P. R. China. E-mail: happyhu@ncu.edu.cn

^d National Center for Nanoscience and Technology, Beijing 100190, P. R. China.

[‡] These authors contributed equally to this work.

Experimental Procedures

Materials

The chemical reagents and materials were purchased and used as received without further purification. lipoic acid (LA) and 1,3-diisopropenylbenzene (DIB) were purchased from Tokyo Chemical Industry. 1-butyl-3-methylimidazolium chloride ionic liquid (IL) was purchased from Shanghai Meni Chemical Technology Co., LTD. Aluminum chloride was obtained from Sinopharm Group Chemical Reagent Co., LTD.

Synthesis of ionic conductive elastomer (ICE)

Multifunctional ionic conductive elastomer (ICE) was prepared by a thermally induced polymerization method. First, 5 g of lipoic acid (LA) was added into a three-neck flask and mechanically stirred under the condition of oil bath heating at 90 °C. LA was formed into linear poly(lipoic acid) (poly(LA)) by ring-opening polymerization of disulfide bonds under the heating condition, and a yellow transparent poly(LA) solution was obtained after 30 min. Then 1 g of 1,3-diisopropenylbenzene (DIB), 0.2 g of 1-butyl-3-methylimidazolium chloride ionic liquid (IL) and 0.01 g of aluminium chloride (AlCl_3) were successively added to the liquid poly(LA), and the copolymerization was completed by continuous stirring for 10 min. After cooling to room temperature, the transparent and flexible ionic conductive gel of ICE was obtained.

Device Fabrication

The rigid Glass/ITO substrates and flexible PEN/ITO substrates, 2,2',7,7'-tetrakis-[N,N-di(4-methoxyphenyl)-amino]-9,9'-spirobifluorene (Spiro-OMeTAD) were purchased from Advanced Election Technology Corp. The tin (IV) oxide (SnO_2) colloid solution was purchased from Alfa Aesar. Anhydrous N, N-dimethylformamide (DMF), anhydrous dimethyl sulfoxide (DMSO), isopropanol (IPA) and chlorobenzene (CB) were obtained from Sigma-Aldrich. Lead iodide (PbI_2), formamidinium iodide (FAI), methylammonium iodide (MAI), methylammonium chloride (MACl), bis(trifluoromethane) sulfonimide lithium salt (LiTFSI) and 4-tertbutylpyridine (tBP) were purchased from Xi'an Polymer Light Technology Corp.

The flexible PEN/ITO substrate was ultrasonic cleaned with detergent/water, distilled water, ethanol and isopropanol for 20 min, then dried with N_2 blowing and treated by ultraviolet-ozone for 30 min. To prepare high-efficiency flexible PSCs, the PEN/ITO substrate was bonded onto the glass substrate coated with PDMS precursors, and then cured at 80 °C for 2 h to prepare the PEN/ITO/glass composite substrate. The SnO_2 film (2.67%) was prepared on the PEN/ITO/glass substrate by using the blade coating technique, in which the coating speed was 15 mm/s, and the distance between the scraper and substrate was 100 μm , and then annealed for 30 min at 120 °C to produce SnO_2 film. The perovskite film was further fabricated by blade coating. The 1.3 mol/mL PbI_2 solution (DMF:DMSO = 4:1) was coated onto SnO_2 film with coating speed of 10 mm/s and the distance between the scraper and the substrate was 150 μm . Then, the substrate coated with perovskite precursors is annealed on a hot plate at 70 °C for 1 min. At the same time, ICE with a relative mass ratio of 0.01wt%, 0.02wt% and 0.03wt% to PbI_2 was added to the lead iodide solution, which was heated and stirred at 60 °C for 2 h, and then coated onto the SnO_2 film with the same process as the PbI_2 film. The second step of the blade coating was to disperse 90 mg of FAI, 6.4 mg of MAI, and 9 mg of MACl mixed organic ammonium salts in 1 mL IPA solution and blade-coated them on PbI_2 film at a coating speed of 15 mm/s with a distance of 200 μm between the scraper and the substrate. Then, it was heated at 130 °C for 15 min under ambient air (30-40% humidity). Next, the Spiro-OMeTAD solution was bladed on the perovskite film (coating speed: 10 mm/s), and the film thickness was about 100 μm . The Spiro-OMeTAD solution consisted of 72.3 mg Spiro-OMeTAD, 18 μL bis(trifluoromethane) sulfonimide lithium salt (LiTFSI) stock solution (520 mg LiTFSI in 1 mL acetonitrile), 30 μL 4-tertbutylpyridine (tBP) and 1 mL chlorobenzene. Finally, an 80 nm-thick Au film was vacuum-deposited as the counter electrode, and the effective area of the device was 0.04 cm^2 .

Films characterization

The surface morphology, cross section morphology and grain size distribution of lead iodide and perovskite films were measured by field emission scanning electron microscope (S-4800, Hitachi, Japan) under 5 kV and 10 mA. The I-V curve of the perovskite film was measured on a four-probe test platform (4200-SCS, Keithley) at voltages of -1 V \rightarrow +1 V. The microscopic morphology and surface potential of perovskite films were tested by atomic force-raman spectroscopy multi-mode scanning probe microscopy (Ntegra Spectra, NT-MDT, Russia). Contact angle test (OCA20, Dataphysics, Germany) was used to observe the hydrophilicity of the film surface. X-ray diffractometer (Ringt-2500, Rigaku, Japan) was used to measure the crystal structure and crystallinity of the film. The Cu target was used as the anode target, the test angle was 10~50°, and the scanning speed was 6°/min. The crystalline orientation of perovskite film was detected by grazing-incidence X-ray diffraction (GIWAXS) instrument (Xeuss 2.0, Xenocs), and the angle of the grazing incidence was 0.3° and exposure time was 300 s. The absorption and transmission properties of perovskite films were tested by UV-visible spectrophotometer (UV-2600, Shimadzu, Japan). The steady-state photoluminescence (PL) and time-resolved PL of perovskite films were measured by steady-state and lifetime spectrometer (FLS980, Edinburgh, UK) at 485 nm excitation. The photoluminescence intensity of the films was observed with a laser scanning confocal (LSCM) microscope (Nikon C2 plus, Nikon, Japan). The interaction between ICE and perovskite films was demonstrated by Fourier transform infrared spectroscopy (Bruker, Tensor-27) and X-ray photoelectron spectroscopy (XPS). The residual strain of perovskite films was measured by grazing-incidence X-ray diffraction (GIXRD) instrument (SmartLab, Rigaku Corporation, Japan) in parallel light mode. In ultrahigh vacuum, the work function and energy band positions of the films can be calculated by means of ultraviolet photoelectron spectroscopy (UPS) test (AXIS ULTRA DLD, Shimadzu/Kratos, Japan).

Devices Characterization

The current density-voltage (J - V) curve of the PSCs was obtained by Keithley 2400 source meter under simulated one solar illumination (AM 1.5G, 100 mW/cm²), and NREL correction was performed by standard silicon solar cells. All tests were taken in a nitrogen glove box. The device is measured by reverse scanning (1.25 V \rightarrow -0.1 V, step 0.02 V) and forward scanning (-0.1 V \rightarrow 1.25 V, step 0.02 V). The effective area of the mask is 0.04 cm², 0.1 cm², 0.4 cm², 0.7 cm² and 1.01 cm², respectively. The external quantum efficiency was obtained by a monochromatic illumination optical system (QE-R, Amazing Light Technology, Taiwan) and calibrated using a standard single crystal silicon diode. The impedance spectra were measured by electrochemical impedance analyzer (PGSTAT302N, Aptar, Switzerland, Germany) under dark condition. A stepper tensile machine (Beijing Zhongke Jiming) was used to test the stability of the devices under different bending radii or different bending cycles. All bending test results were obtained from the average of 50 samples.

Figures and Tables

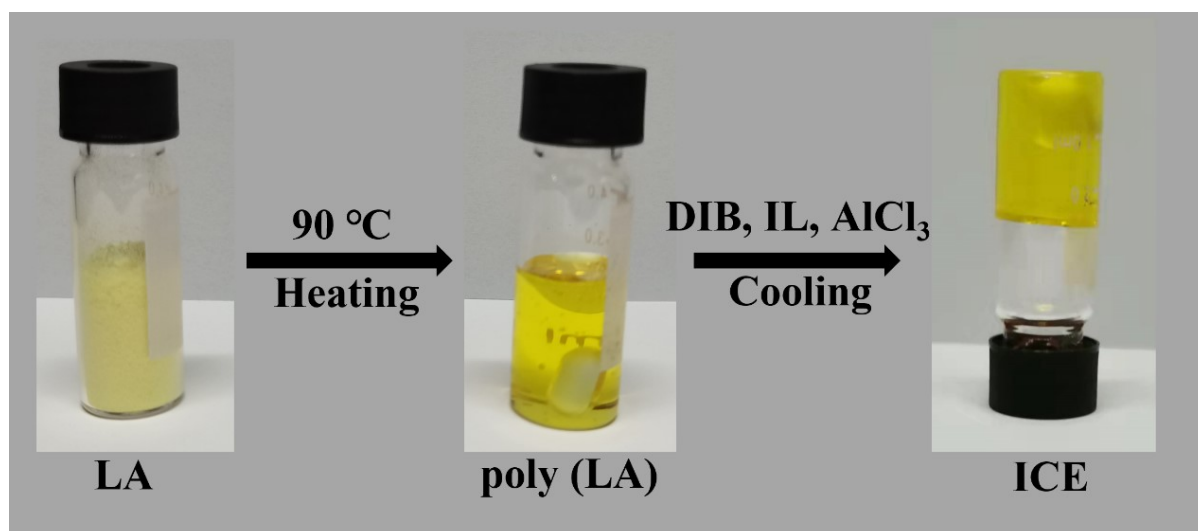


Fig. S1 Photographs of lipoic acid (LA) powder, molten LA liquid (poly (LA)), and ionic conductive elastomers (ICE).

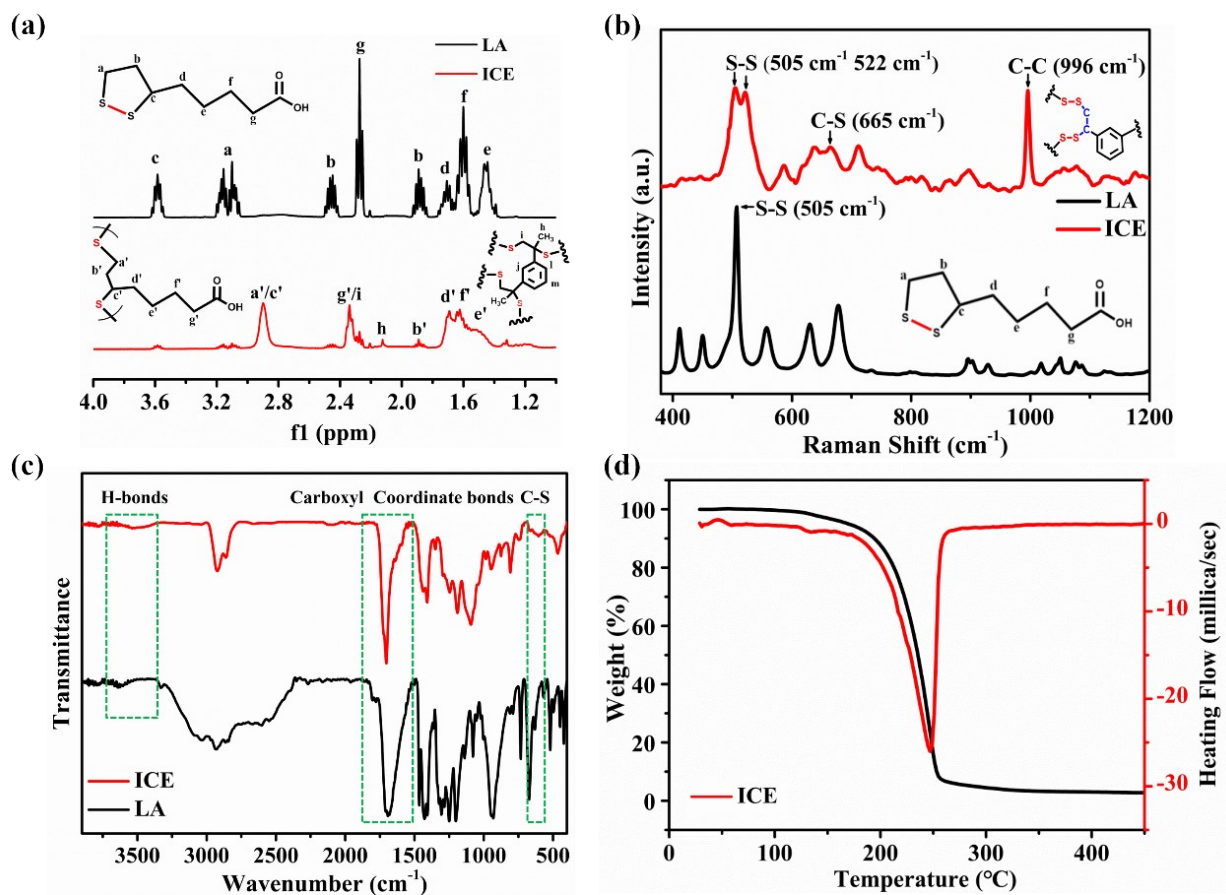


Fig. S2 (a) $^1\text{H-NMR}$ partial spectra of LA monomer (black line) and ICE (red line) with acetone as solvent. (b) Raman spectra of LA monomer (black line) and ICE (red line). (c) FT-IR spectra of LA monomer (blue line) and ICE (red line). (d) The TG and DTG curves of ICE. The ICE exhibits excellent thermostability with the decomposition temperature up to $250\text{ }^{\circ}\text{C}$, much higher than the processing temperatures ($\sim 130\text{ }^{\circ}\text{C}$) for the perovskite films in our experiments, making ensure that the ICE remains in the perovskite films after the processing.

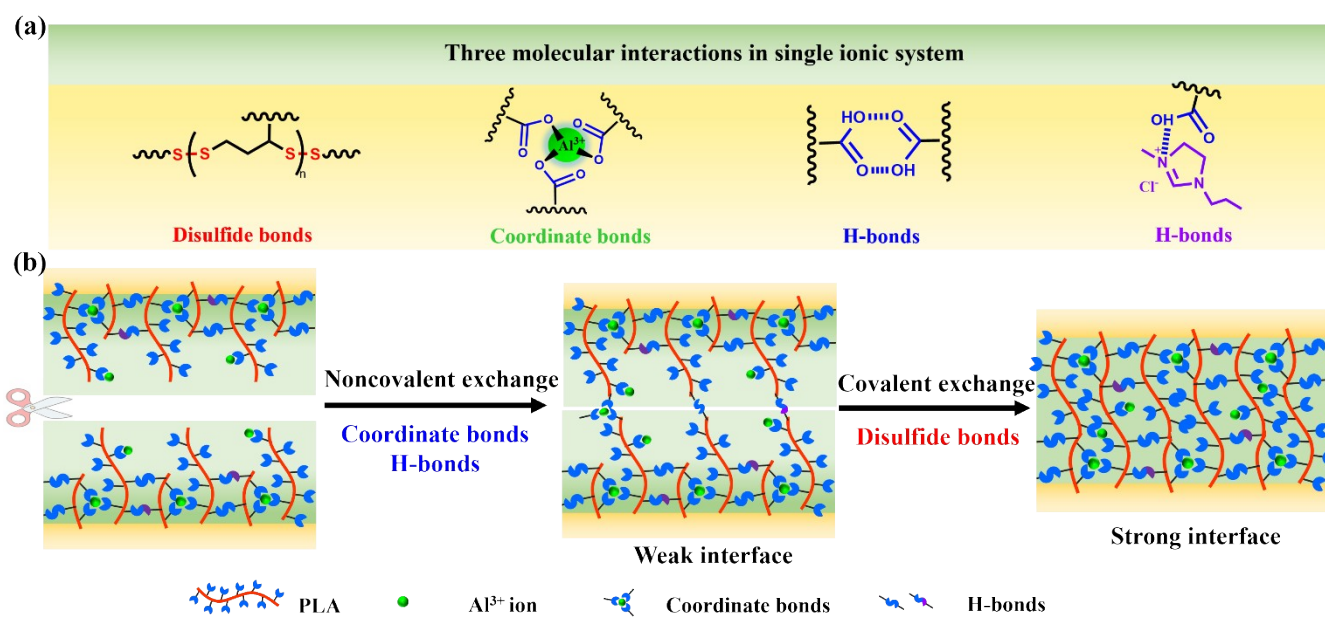


Fig. S3 (a) Schematic of the three molecular interactions in ICE. (b) Schematic of the self-healing process of ICE. During the self-healing process, the hydrogen bonds and coordination bonds is recombined to form a new weak interface through non-covalent interaction. Then, the dynamic disulfide bonds are covalently exchanged along the migration direction of the polymer chain, and the strong interface formed promotes the reconstruction of the polymer network.^{1,2}

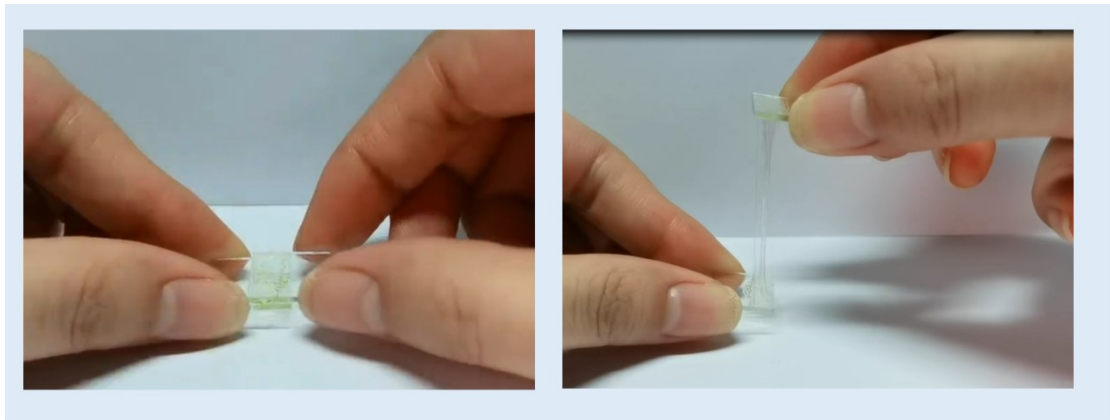


Fig. S4 Photographs of the stretchable viscous ICE adhered between the two glass slices. The ICE was first preheated to the viscous state and then deposited onto glass surfaces.

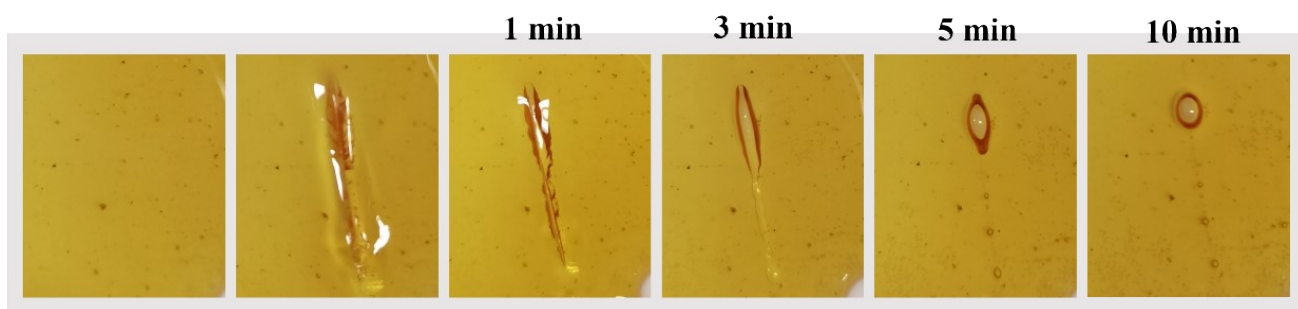


Fig. S5 Photographs depict that a scratch on the ICE membrane can be autonomously cured after 10 min at room temperature.

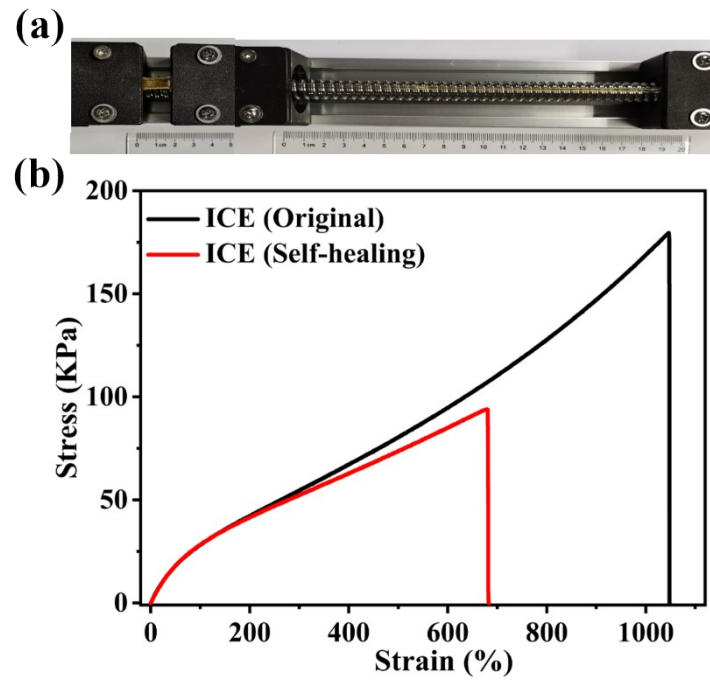


Fig. S6 (a) Photographs of the ICE film before and after stretching. (b) Stress-strain curves of the healed ICE samples with freshly cut interfaces.

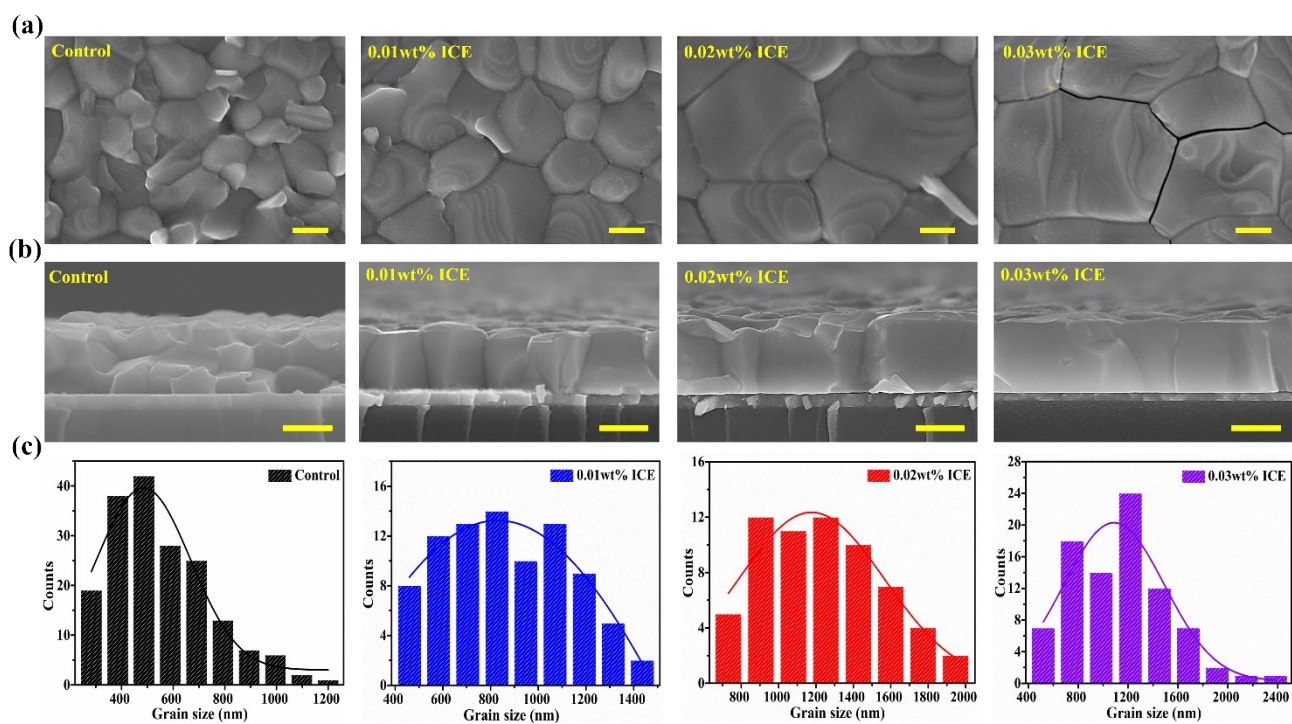


Fig. S7 Surface and cross-section scanning electron microscope (SEM) images and corresponding histogram of final grain size for the perovskite film with different concentrations of ICE (Scale bar: 500 nm).

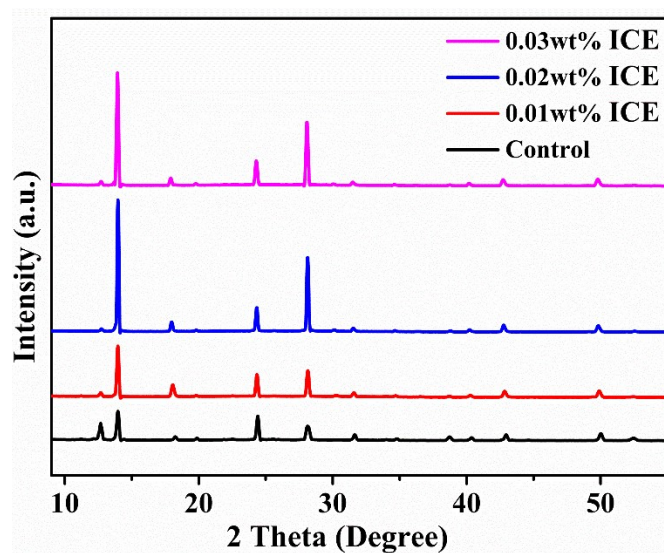


Fig. S8 XRD patterns of perovskite film with different concentrations of ICE. It is found that the remarkable lead iodide (PbI_2) peak of the perovskite film with ICE located at 12.7° is obviously weakened or disappeared, and the highest intensity of diffraction peak was observed for the perovskite films with 0.02wt% ICE. This result indicates that the ICE polymer network can fully react the excess PbI_2 and enhance the crystalline properties of the perovskite films. Therefore, 0.02wt% ICE is the most suitable addition amount.

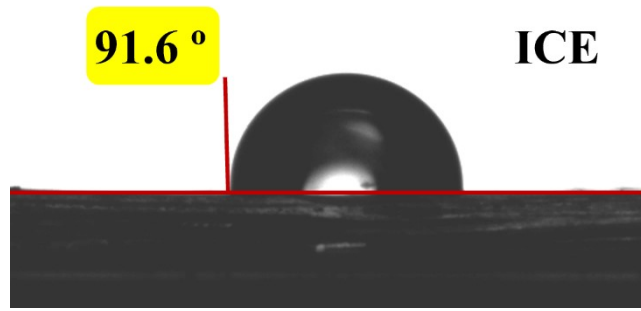


Fig. S9 Water contact angle of perovskite films with ICE.

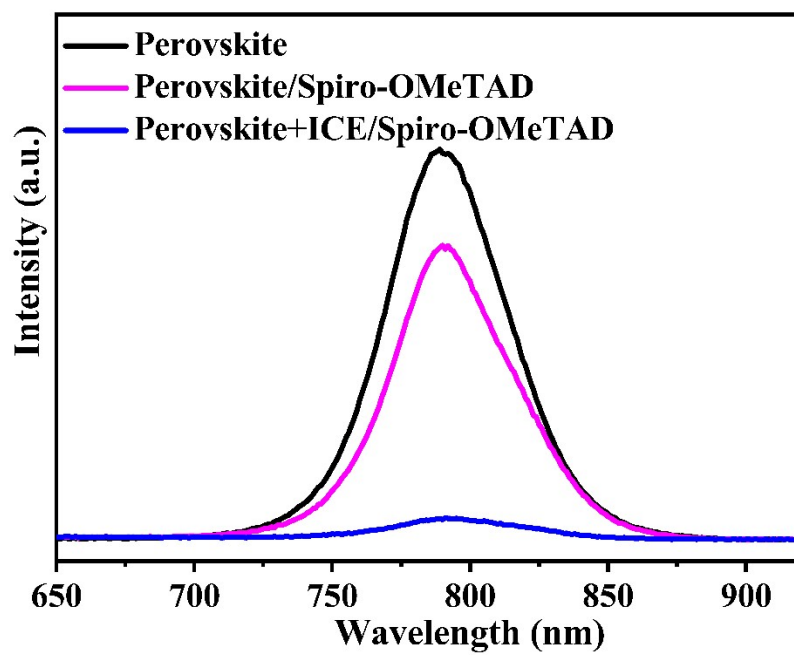


Fig. S10 Steady-state photoluminescence emission spectra of perovskite, perovskite/Spiro-OMeTAD and perovskite+ICE/Spiro-OMeTAD.

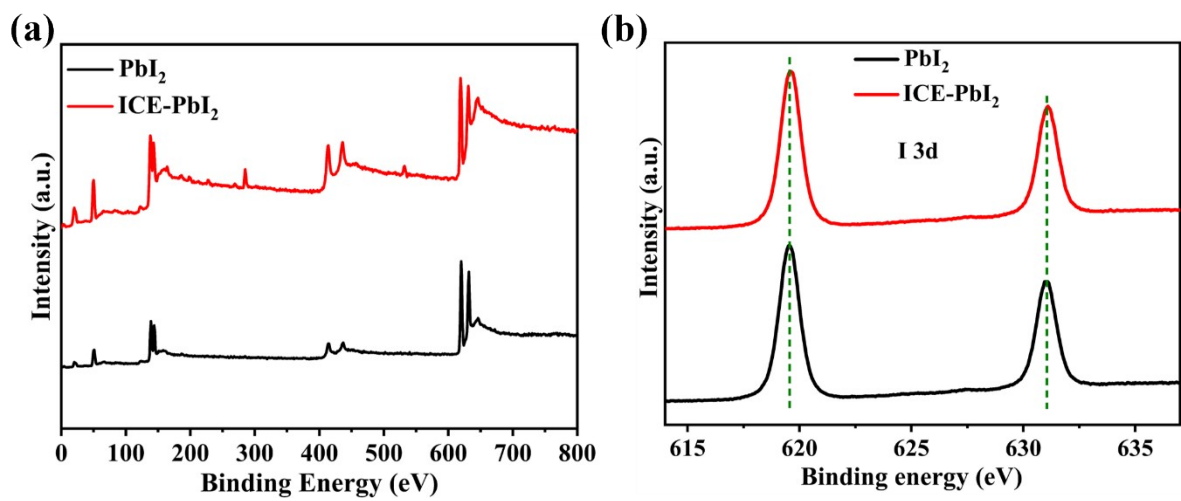


Fig. S11 XPS spectra of (a) entire elements; (b) I 3d of the PbI_2 and ICE- PbI_2 film.

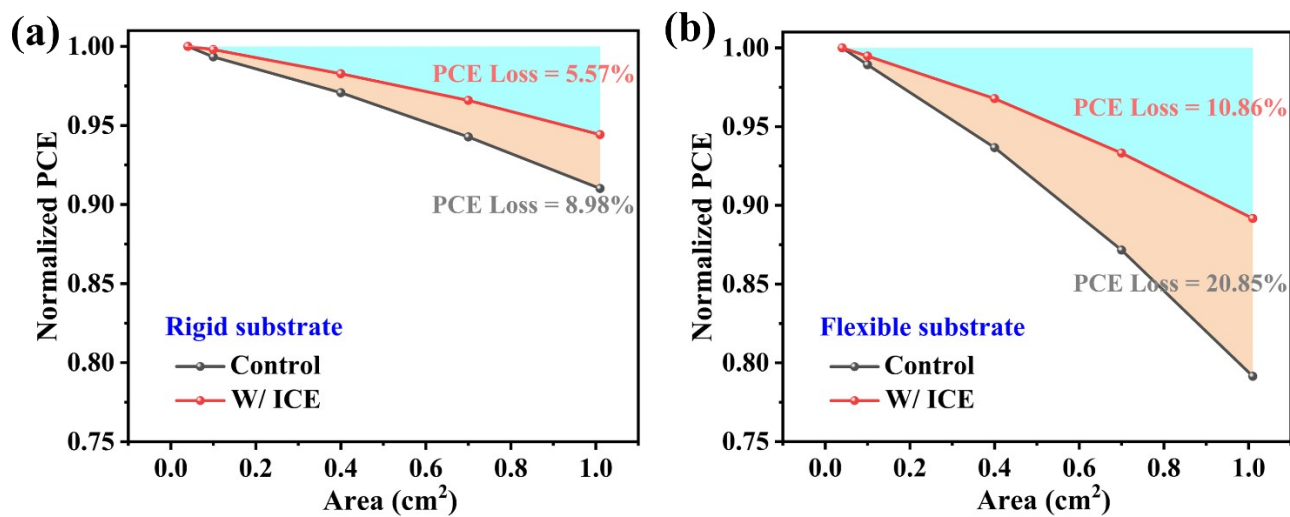


Fig. S12 The relationship between the active area and PCE loss for the PSCs based on (a) the rigid substrate and (b) flexible substrate.

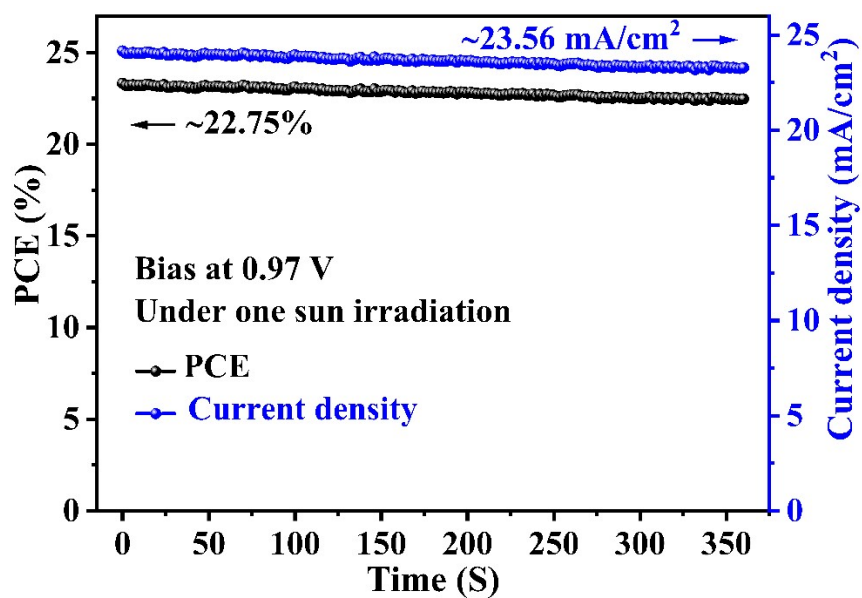


Fig. S13 The stabilized output power and photocurrent of the control flexible PSCs measured under a constant bias voltage (0.97 V) near the maximum power point.

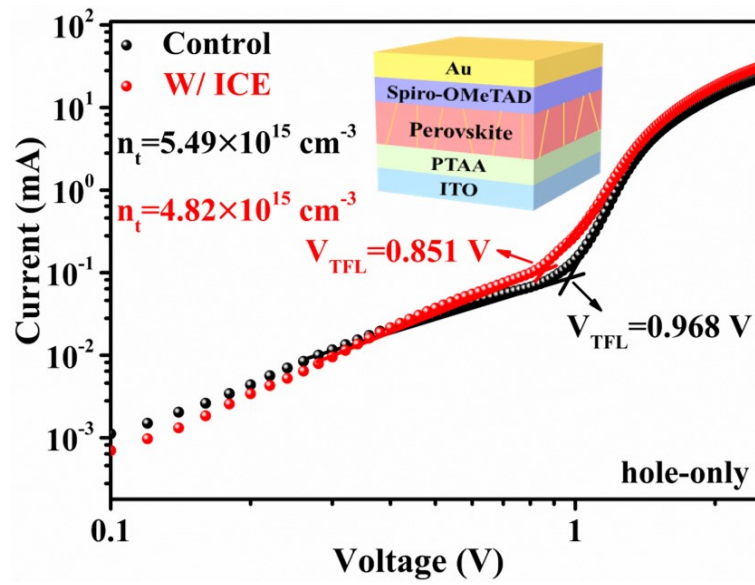


Fig. S14 Dark J - V curves of the SCLC measurements based on the hole-only device (ITO/PTAA/perovskite/Spiro-OMeTAD/Au) for the PSCs.

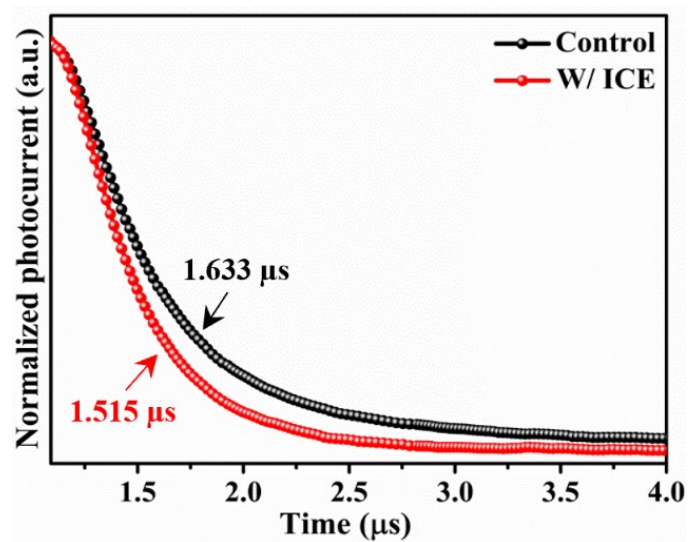


Fig. S15 The transient photocurrent (TPC) curves of the control and ICE-containing PSCs.

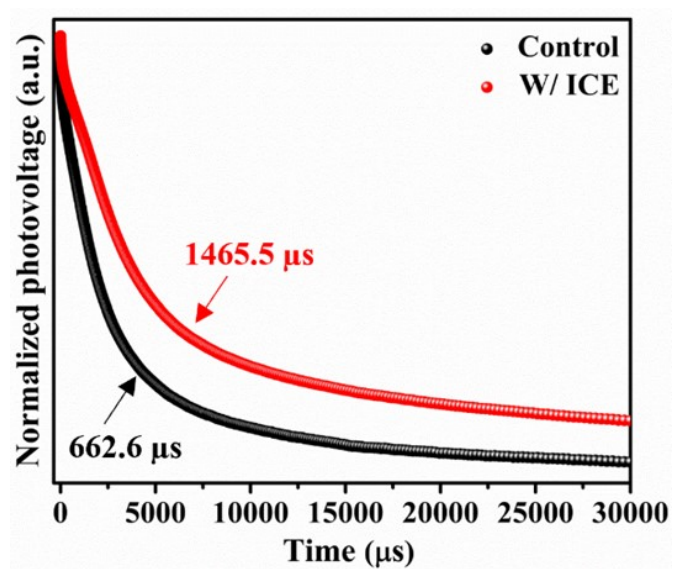


Fig. S16 The transient photovoltage (TPV) curves of the control and ICE-containing PSCs.

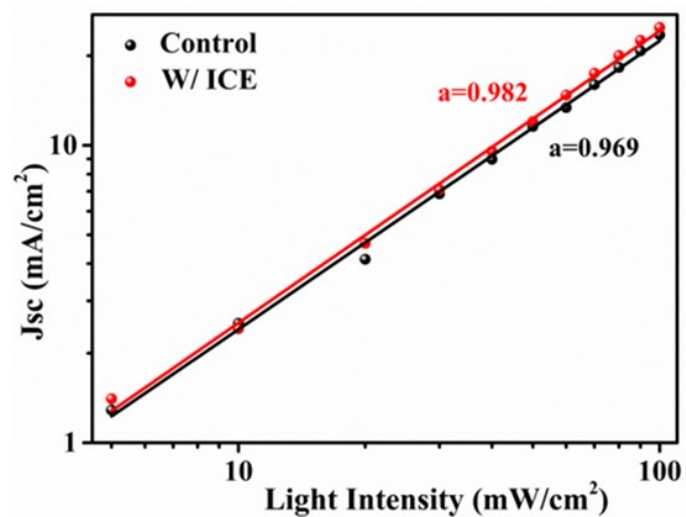


Fig. S17 The relationship between the measured J_{sc} and light intensity of the control and ICE-containing PSCs.

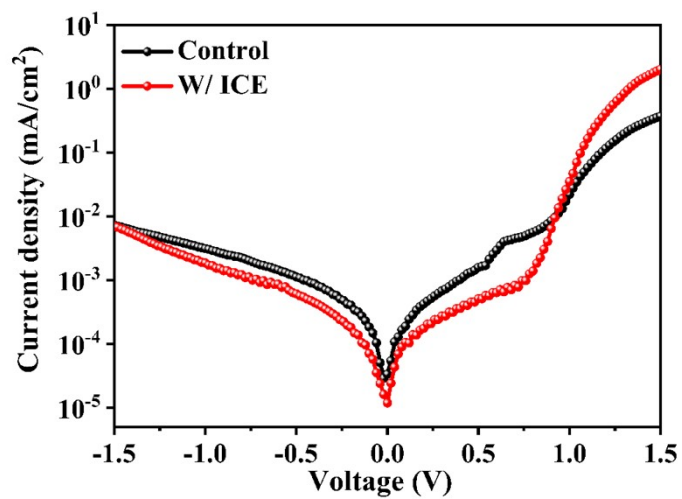


Fig. S18 Dark *J-V* curves of the control and ICE-containing PSCs.

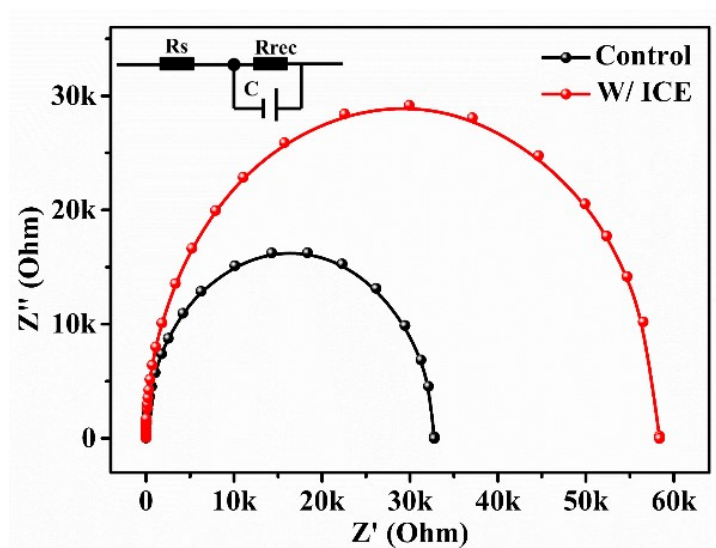


Fig. S19 Electrical impedance spectroscopy (EIS) of the control and ICE-containing PSCs in dark.

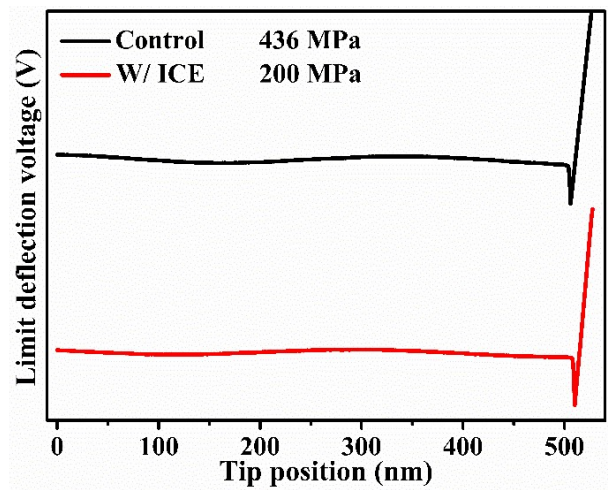


Fig. S20 Young's Modulus of the control and ICE-containing perovskite films measured by the peak-force model of AFM.

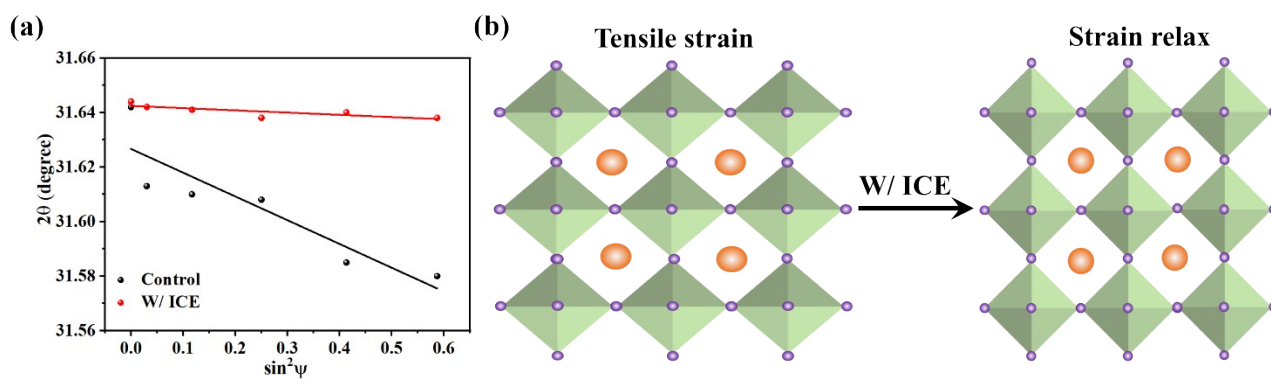


Fig. S21 (a) $2\theta \sim \sin^2\psi$ fitting residual strain of the control and ICE-containing perovskite films. (b) Schematic illustration of the ICE-containing perovskite films to release the strain.

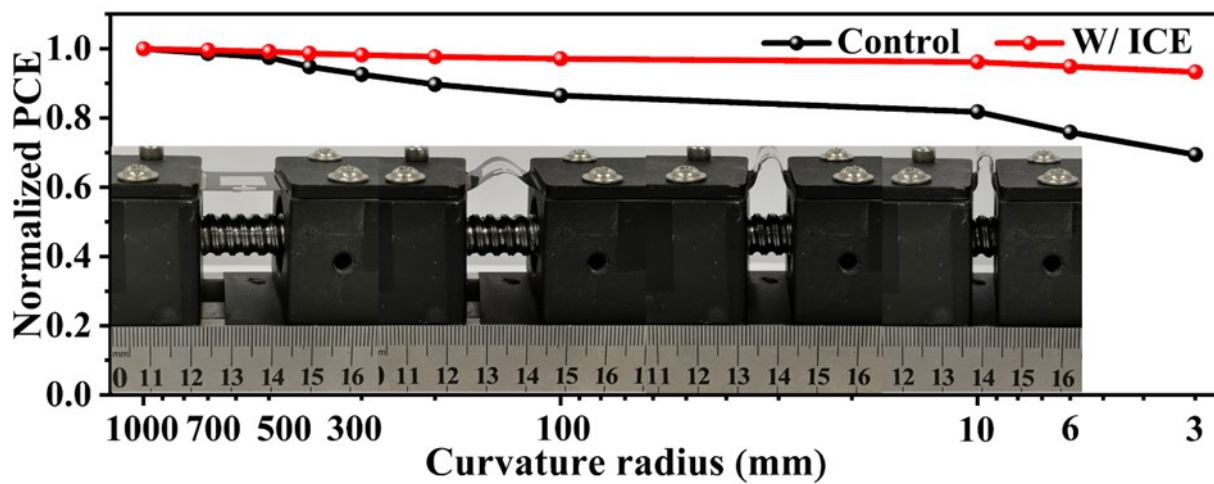


Fig. S22 Normalized average PCE of flexible PSCs measured after bending 1000 cycles within a curvature radius from flat to 3 mm.

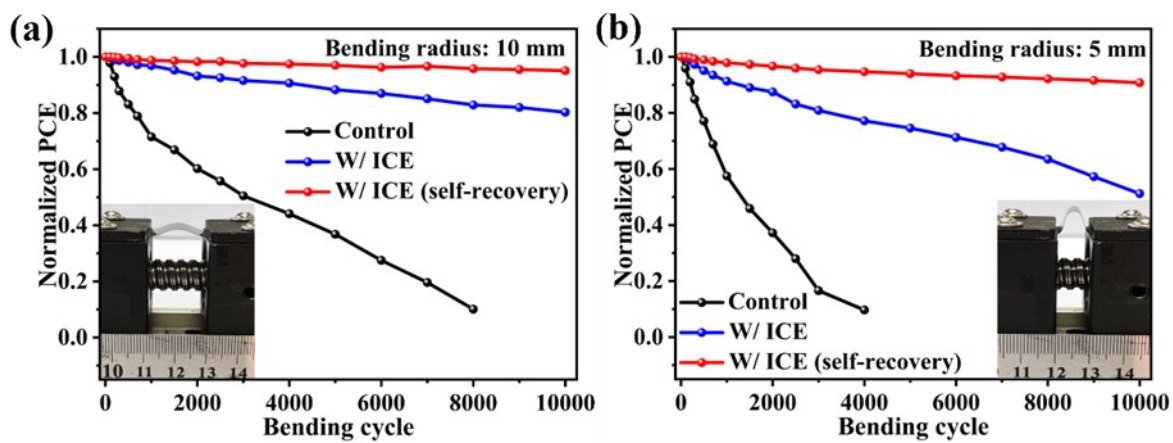


Fig. S23 Normalized average PCE of PSCs as a function of bending cycles with bending radius of (a) 10 mm and (b) 5 mm. Normalized average PCE of PSCs as a function of bending cycles with bending radius of (a) 10 mm and (b) 5 mm.

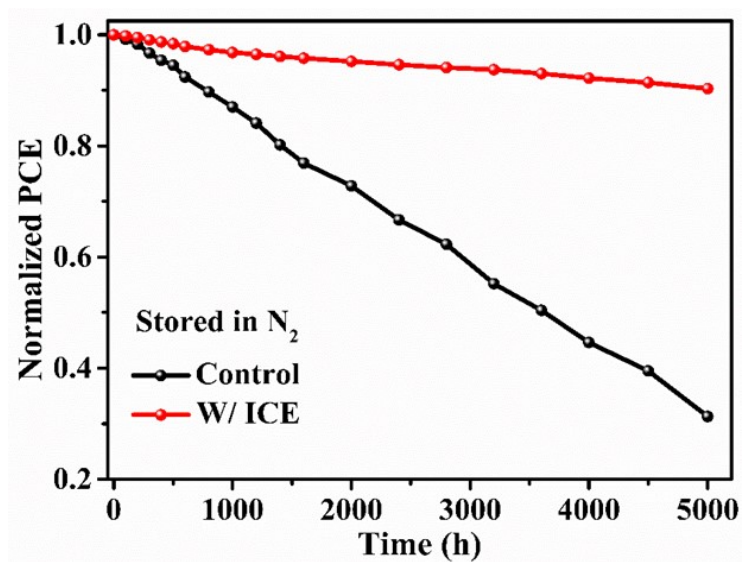


Fig. S24 Long-term stability of devices over 5000 h stored in the N₂ glove box.

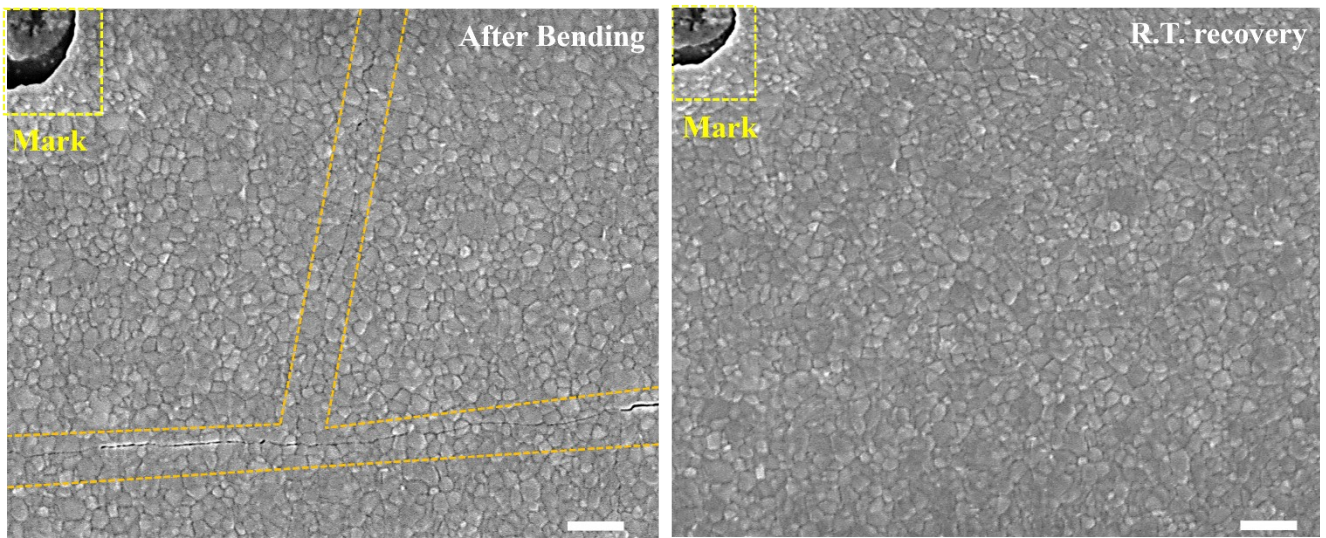


Fig. S25 In situ SEM images of perovskite film with mechanical crack before and after self-recovery (Scale bar: 2 μm).

Grain boundaries cracks

Room Temperature Self-healing

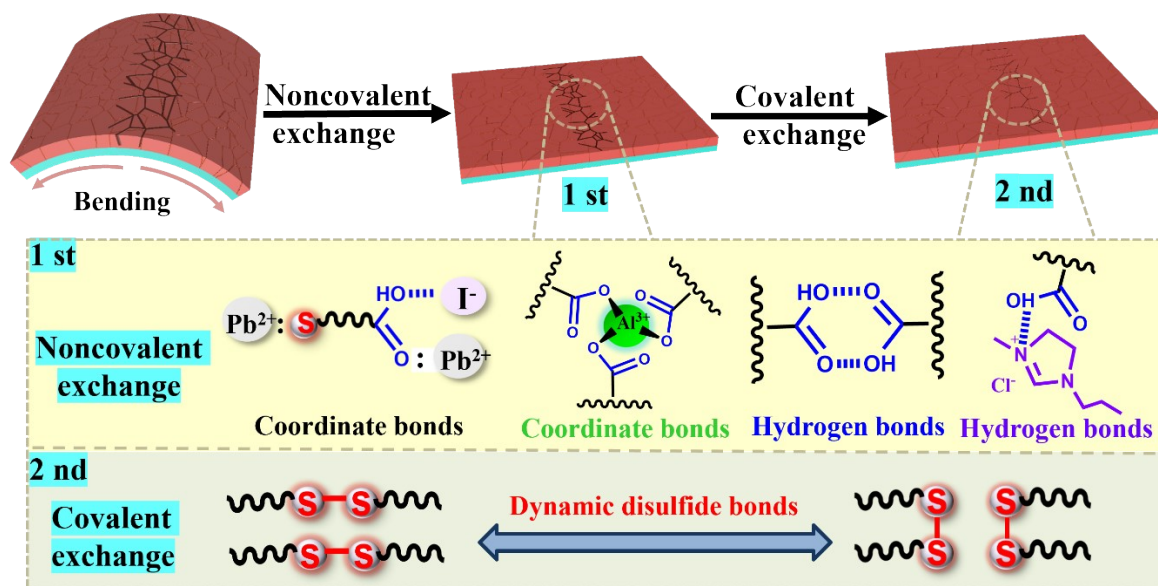


Fig. S26 Schematic of the self-healing process of the ICE-containing perovskite film. Based on the strong dynamic self-healing properties of ICE distributed at the grain boundaries, the non-covalent dynamic hydrogen bonds and metal coordination bonds of the ICE are reconstructed, and then the disulfide bonds are dynamically rearranged to complete the reconstruction of the polymer network, so as to self-repair the grain boundaries cracks of the perovskite film after 1 h (~25 °C).

Table S1. τ_1 and τ_2 from PL decay spectra with different samples.

Samples	τ_1 (ns)	A_1 (%)	τ_2 (ns)	A_2 (%)	τ(ns)
Control	62.36	35.64	165.87	64.36	128.98
W/ICE	57.17	1.23	387.99	98.77	383.92

The PL decay fitting curve is based on a bi-exponential rate law:

$$f(t) = A_1 \exp(-t/\tau_1) + A_2 \exp(-t/\tau_2) + \gamma_0$$

Where A_1 and A_2 represent the decay amplitude, τ_1 represents trap-assisted recombination, and τ_2 demonstrates free carrier recombination, and γ_0 is a constant.

Table S2. Device parameters of the Rigid PSCs.

Device ^{a)}	J_{sc} [mA/cm ²]	V_{oc} [V]	FF	PCE [%]
Reverse scan Control	25.30	1.181	0.812	24.27
Forward scan Control	25.12	1.179	0.803	23.83
Average	25.00±0.50	1.180±0.007	0.790±0.025	23.85±0.80
Reverse scan W/ICE	25.92	1.190	0.826	25.47
Forward scan W/ICE	25.80	1.188	0.815	25.08
Average	25.70±0.30	1.187±0.005	0.815±0.015	25.10±0.50

Table S3. Photovoltaic parameters of the rigid PSCs with different active area.

Device	Area [cm ²]	J_{sc} [mA/cm ²]	V_{oc} [V]	FF	PCE [%]
Control	0.04	25.30	1.181	0.812	24.27
	0.1	25.28	1.180	0.808	24.11
	0.4	25.17	1.171	0.799	23.56
	0.7	25.01	1.161	0.787	22.88
	1.01	24.84	1.148	0.773	22.09
W/ICE	0.04	25.92	1.190	0.826	25.47
	0.1	25.91	1.191	0.824	25.42
	0.4	25.82	1.184	0.818	25.03
	0.7	25.77	1.175	0.812	24.60
	1.01	25.59	1.165	0.806	24.05

Table S4. Photovoltaic parameters of the flexible PSCs with different active area.

Device	Area [cm ²]	J_{sc} [mA/cm ²]	V_{oc} [V]	FF	PCE [%]
Control	0.04	24.68	1.183	0.794	23.21
	0.1	24.55	1.181	0.792	22.96
	0.4	24.23	1.168	0.767	21.74
	0.7	24.11	1.152	0.728	20.23
	1.01	23.98	1.133	0.676	18.37
W/ICE	0.04	25.39	1.190	0.821	24.84
	0.1	25.28	1.189	0.821	24.71
	0.4	24.89	1.182	0.816	24.04
	0.7	24.78	1.171	0.798	23.18
	1.01	24.56	1.157	0.779	22.15

Table S5. Summary of self-repairing flexible perovskite solar cells.

Self-healing material	Self-healing mechanism	Self-healing condition	Performance	Performance after healing	Ref.
Polyurethane (PU)	Dynamic disulfide bond	80 °C	10.16% PCE, 28 h at 50% RH and 25 °C	90% of initial PCE	3
TUEG ₃ polymer	Hydrogen bond	100 °C, 1 h	13.6% PCE	80% of initial PCE	4
Polyurethane with disulfide bonds (PUDS)	Disulfide bond	80 °C, 10 min	17.19% PCE, 1000 cycles at bending	88% of initial PCE	5
α -lipoic acid (LA)	Disulfide bond	65 °C, 6 h	19.03% PCE, 3000 cycles at bending	95% of initial PCE	6
Polyurethane (s-PU)	Dynamic oxime-carbamate bond	100 °C, 10 min	19.15% PCE, 1000 cycles at 20% stretch	88% of initial PCE	7
Self-healing polysiloxane (SHP)	Coordination units and hydrogen bonds	R.T., 2 h	19.50% PCE, 150 cycles at 20% stretch	80% of initial PCE	8
MAGH, GMA- β -CD and N-AA ternary prepolymer (TPP)	Host-guest interaction	60-70% RH, 4 h	20.46% PCE, 4000 cycles at bending	90% of initial PCE	9
Poly(acrylamide-nbutyl acrylate) AD-23	Hydrogen-bond	70 °C, 5 min	20.50% PCE, 500 cycles at bending	20.23% PCE	10
Shape memory polyurethane (SMPU)	Shape memory and hydrogen bonding	37 °C, 30 min	21.33% PCE, 3000 cycles at bending	91% of initial PCE	11
Fullerene derivatized polyurethane (C60-PU)	Disulfide bond	80 °C, 10 min	21.36% PCE, 500 h at 50% RH and 25 °C	78% of initial PCE	12
Ionogel (IG)	Dynamic hydrogen bonds	R.T., 10 h	21.76% PCE 1000 cycles at bending	90% of initial PCE	13
Dynamic supramolecular PDMS polyurethane (DSSP-PPU)	Disulfide bond exchange and multiple hydrogen bonds	R.T., 1 h	22.24% PCE, 8000 cycles at bending	~90% of initial PCE	14
(5-(1,2-dithiolan-3-yl) pentanehydrazide hydroiodide (TA-NI)	Dynamic covalent disulfide bonds, H-bonds, and ammonium	35 °C, 1 h	23.84% PCE (0.062 cm ²) and 21.66% PCE (1.004 cm ²) 4000 cycles at bending	97% of initial PCE	15
Ionic conductive elastomer (ICE)	Dynamic covalent disulfide bonds, multiple hydrogen bonds and metal coordination bonds	R.T. (25 °C), 1 h	24.84% PCE (0.04 cm²) 10000 cycles at bending	91% of initial PCE	This work

References

- [1] Q. Zhang, C.-Y. Shi, D.-H. Qu, Y.-T. Long, B. L. Feringa, H. Tian, *Sci. Adv.* 2018, **4**, eaat8192.
- [2] C. Dang, M. Wang, J. Yu, Y. Chen, S. Zhou, X. Feng, D. Liu, H. Qi, *Adv. Funct. Mater.* 2019, **29**, 1902467.
- [3] Q. Zhang, J. Duan, Q. Guo, J. Zhang, D. Zheng, F. Yi, X. Yang, Y. Duan, Q. Tang, *Angew. Chem. Int. Ed.* 2022, **61**, e202116632.
- [4] B. P. Finkenauer, Y. Gao, X. Wang, Y. Tian, Z. Wei, C. Zhu, D. J. Rokke, L. Jin, L. Meng, Y. Yang, L. Huang, K. Zhao, L. Dou, *Cell Rep. Phys. Sci.* 2021, **2**, 100320.
- [5] Y. Lan, Y. Wang, Y. Lai, Z. Cai, M. Tao, Y. Wang, M. Li, X. Dong, Y. Song, *Nano Energy* 2022, **100**, 107523.
- [6] J. Yang, W. Sheng, X. Li, Y. Zhong, Y. Su, L. Tan, Y. Chen, *Adv. Funct. Mater.* 2023, **33**, 2214984.
- [7] X. Meng, Z. Xing, X. Hu, Z. Huang, T. Hu, L. Tan, F. Li, Y. Chen, *Angew. Chem. Int. Ed.* 2020, **59**, 16602-16608.
- [8] K. Zhang, Y. Deng, X. Shi, X. Li, D. Qi, B. Jiang, Y. Huang, *Angew. Chem. Int. Ed.* 2021, **60**, 2-9.
- [9] Z. Yang, Y. Jiang, D. Xu, Z. Wang, X. Gao, X. Lu, G. Zhou, J.-M. Liu, J. Gao, *J. Mater. Chem. A* 2022, **10**, 22445-22452.
- [10] C. Ge, X. Liu, Z. Yang, H. Li, W. Niu, X. Liu, Q. Dong, *Angew. Chem. Int. Ed.* 2022, **61**, e202116602.
- [11] T. Xue, Z. Huang, P. Zhang, M. Su, X. Hu, T. Wu, B. Fan, G. Chen, G. Yu, W. Liu, X. Liu, Y. Zhang, Y. Song, *InfoMat* 2022, **4**, e12358.
- [12] T. Zheng, Q. Zhou, T. Yang, Y. Zhao, B. Fan, J. Bo, L. Fan, R. Peng, *Carbon* 2022, **196**, 213-219.
- [13] Y. Kang, R. Li, A. Wang, J. Kang, Z. Wang, W. Bi, Y. Yang, Y. Song, Q. Dong, *Energy Environ. Sci.* 2022, **15**, 3439-3448.
- [14] Z. Yang, Y. Jiang, Y. Wang, G. Li, Q. You, Z. Wang, X. Gao, X. Lu, X. Shi, G. Zhou, J. M. Liu, J. Gao, *Small* 2023, 2307186.
- [15] Z. Chen, Q. Cheng, H. Chen, Y. Wu, J. Ding, X. Wu, H. Yang, H. Liu, W. Chen, X. Tang, X. Lu, Y. Li, Y. Li, *Adv. Mater.* 2023, **35**, 2300513.